

Early Stopping for Deep Image Prior

Hengkang Wang Taihui Li Zhong Zhuang Tiancong Chen Hengyue Liang Ju Sun
Department of Computer Science and Engineering
Department of Electrical and Computer Engineering
University of Minnesota, Twin Cities

{wang9881, lixx5027, zhuan143, chen6271, liang656, jusun}@umn.edu

Abstract

Deep image prior (DIP) and its variants have showed remarkable potential for solving inverse problems in computer vision, without any extra training data. Practical DIP models are often substantially overparameterized. During the fitting process, these models learn mostly the desired visual content first, and then pick up the potential modeling and observational noise, i.e., overfitting. Thus, the practicality of DIP often depends critically on good early stopping (ES) that captures the transition period. In this regard, the majority of DIP works for vision tasks only demonstrates the potential of the models—reporting the peak performance against the ground truth, but provides no clue about how to operationally obtain near-peak performance without access to the groundtruth. In this paper, we set to break this practicality barrier of DIP, and propose an efficient ES strategy, which consistently detects near-peak performance across several vision tasks and DIP variants. Based on a simple measure of dispersion of consecutive DIP reconstructions, our ES method not only outpaces the existing ones—which only work in very narrow domains, but also remains effective when combined with a number of methods that try to mitigate the overfitting. The code is available at https://github.com/sun-umn/Early_Stopping_for_DIP.

1. Introduction

Inverse problems (IPs) are prevalent in computer vision, from basic image denoising, super-resolution, deblurring, to advanced 3D reconstruction and major tasks in computational photography and imaging [37]. Despite the disparate settings, all these problems take the form of recovering a visual object \mathbf{x} from $\mathbf{y} = f(\mathbf{x})$, where f models the forward process to obtain the observation \mathbf{y} . Typically, these visual IPs are underdetermined: \mathbf{x} cannot be uniquely determined from \mathbf{y} . This is exacerbated by potential modeling (e.g., linear f to approximate a nonlinear process) and observational

(e.g., Gaussian or Shot) noise, i.e., $\mathbf{y} \approx f(\mathbf{x})$. To overcome the nonuniqueness and improve noise stability, people often encode a variety of problem-specific priors on \mathbf{x} when formulating IPs.

Traditionally, IPs are phrased as regularized data-fitting:

$$\min_{\mathbf{x}} \underbrace{\ell(\mathbf{y}, f(\mathbf{x}))}_{\text{data-fitting}} + \lambda \underbrace{R(\mathbf{x})}_{\text{regularizer (reg.)}} \quad \lambda : \text{reg. parameter.} \quad (1)$$

Here, the loss ℓ is chosen according to the noise model, and the regularizer R encodes priors on \mathbf{x} . The advent of deep learning (DL) has revolutionized how IPs are solved: on the radical side, deep neural networks (DNNs) are trained to directly map any given \mathbf{y} to an \mathbf{x} ; on the mild side, pre-trained DL models are taken to replace certain nonlinear mappings in optimization algorithms to solve (1) (e.g., plug-and-play, and algorithm unrolling). We refer the reader to surveys [19, 31] on these developments, which trust large training sets $\{(\mathbf{y}_i, \mathbf{x}_i)\}$ to sufficiently represent the underlying priors and/or noise distributions. *This paper concerns another family of striking ideas, that parametrize \mathbf{x} using DNNs and require no extra training data.*

Deep image prior (DIP) [40] The idea is simple: parametrize \mathbf{x} as $\mathbf{x} = G_{\theta}(\mathbf{z})$, where G_{θ} is a trainable DNN parametrized by θ and \mathbf{z} is a trainable or frozen random seed, put it into (1), and optionally remove the regularizer:

$$\min_{\theta} \ell(\mathbf{y}, f(G_{\theta}(\mathbf{z}))). \quad (2)$$

The DNN G_{θ} is often significantly “overparameterized”—containing substantially more parameters than the dimension of \mathbf{x} , and the resulting optimization problem is solved via standard first-order methods for modern DL (e.g., (adaptive) gradient descent). When \mathbf{x} contains multiple components with different physical meanings, one can naturally parametrize \mathbf{x} using multiple DNNs.

The simple procedure has produced surprisingly competitive recovery results on a myriad of visual IPs, from

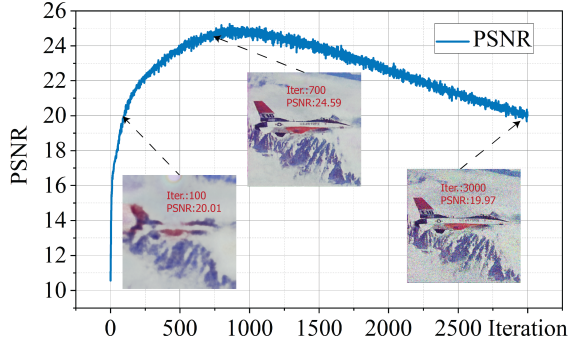


Figure 1. The ELTO phenomenon for DIP.

low-level image denoising, super-resolution, inpainting [14, 25, 40] and blind deconvolution [2, 33, 39, 42], to mid-level image decomposition [10] and image fusion [26], and to advanced computational imaging problems [3, 4, 8, 11–13, 41, 43, 44] (see the survey [32]). A salient feature of the procedure is *no extra training data*, despite the presence of DNNs: the G_θ 's—often convolutional neural networks (CNNs)—are chosen to simply enforce structural priors for natural visual objects.

Overfitting issue in DIP A critical detail we glossed over above is *overfitting*. Since G_θ is substantially overparameterized, $G_\theta(z)$ can in principle represent arbitrary elements in the x domain. Globally optimizing (2) would normally lead to $y = f(G_\theta(z))$, but a priori the reconstruction $G_\theta(z)$ may not reproduce x : this can happen when, e.g., f is non-injective, or $y \approx f(x)$ so that $G_\theta(z)$ also accounts for modeling and observational noise.

Fortunately, the combination of DIP models and first-order optimization methods offers a blessing: in practice, $G_\theta(z)$ has a bias toward the desired visual content, and learns it much faster than learning the noise. So the reconstruction quality climbs to a peak before potential degradation due to noise; see Fig. 1. This “early-learning-then-overfitting” (ELTO) phenomenon has been repeatedly reported, and is also backed by theories on simple G_θ and linear f [15, 16]. The successes of DIP models claimed above are mostly conditioned on the premise that *early stopping* (ES) around the performance peak can be made.

Prior work addressing the overfitting However, without the groundtruth x , we cannot compute the performance curve. One can possibly resort to visual inspection, but this quickly becomes infeasible for many scenarios, such as (1) large-scale batch processing, (2) recovery of visual contents tricky to be visualized and/or examined by eyes (e.g., 3D or 4D visual objects), and (3) scientific imaging of unfamiliar objects (e.g., MRI imaging of rare tumors, and microscopic imaging of new virus species). Overall, there are mainly

three lines of research addressing the overfitting issue.

- **Regularization:** [14] mitigates overfitting by restricting the size of G_θ into the underparameterization regime. [5, 20, 28, 34] control the network capacity by regularizing the layerwise weight norms or the network Jacobian of G_θ . [4, 25, 27, 36] use additional regularizer(s) $R(G_\theta(z))$, such as total-variation norm or trained denoisers, to favor “simple” reconstructions. However, in general it is difficult to choose the right regularization level to preserve the peak performance while avoiding overfitting, and the optimal λ likely depends on the noisy type and level, as shown in Sec. 3.1—the default λ 's for selected methods in this category still lead to overfitting for high-level noise.
- **Noise modeling:** [45] models sparse additive noise as an explicit term in their optimization objective. [20] designs Gaussian- and Shot-specific regularizers and ES criteria. [9] explores subgradient methods with diminishing a step size schedule for impulse noise with the ℓ_1 loss, with preliminary success. These methods do not work beyond the noise types and levels they target, whereas our knowledge about noise in a given visual object is typically limited.
- **Early stopping (ES):** Very recently, several works perform ES directly. [34] tracks the progress based on a ratio of no-reference blurriness and sharpness, but the criterion only works for their modified DIP models, as knowledgeable by the authors and confirmed in Sec. 3.1. [20] provides noise-specific regularizer and ES criterion as alluded to above, but it is unclear how to extend the methods to unknown noise types and levels. Most close to the current work is [23], from a subset of the current authors. There, we propose monitoring the DIP reconstruction quality by training a coupled autoencoder. Although it leads to similar detection performance to the method we propose below, the extra autoencoder training slows down the whole process dramatically; see Sec. 3. [9] effectively also performs ES, where the iteration stalls when the step size becomes negligible.

Our contribution In this paper, we advocate the ES approach for practicality reasons: (1) The regularization and noise modeling approaches, even if effective, often do not improve the peak performance but push it until the last iterations; there could be $\geq 10\times$ more iterations spent than that of climbing to the peak in the original DIP models; (2) Both approaches operate on the basis of deep or even precise knowledge about the noise type and level, which are practically unknown for most applications. If their key models and hyperparameters are not set appropriately, overfitting likely remains. Then one still needs to perform ES.

We propose a novel ES criterion for DIP models by tracking the trend of the dispersion of consecutive reconstructions. Our ES method is

- **Effective:** The gap between our detected and the peak performance, i.e., detection gap, is typically very small, as measured by standard visual quality metrics;
- **Efficient:** It is lightweight, and the per-iteration overhead is negligible relative to the per-iteration cost of optimizing problem (2);
- **General:** Our method works well for DIP and its variants (including DD [14] and SIREN [35]), different noise types and levels, and across a number of visual IPs. Also, our method can be wrapped around several regularization methods, e.g., GP-DIP [6], DIP-TV [4,25] to perform reasonable ES when they fail to prevent overfitting.
- **Robust:** Our method is relatively insensitive to the two hyperparameters, i.e., window size and patience number (see Secs. 2 and 3.4). By contrast, the hyperparameters of most methods we reviewed above are sensitive to the noise type and level.

2. Our early-stopping (ES) method

We assume this setup: $\mathbf{x} \in \mathbb{R}^{n \times n}$ is the groundtruth but unknown to us. We observe the variable sequence $\{\boldsymbol{\theta}^t\}_{t \geq 1}$, and the corresponding reconstruction sequence $\{\mathbf{x}^t\}_{t \geq 1}$, where $\mathbf{x}^t \doteq G_{\boldsymbol{\theta}^t}(\mathbf{z})$. The performance is measured in terms of PSNR: for any $\mathbf{x}' \in \mathbb{R}^{n \times n}$, $\text{PSNR}(\mathbf{x}') = 10 \log_{10} \|\mathbf{x}\|_{\infty}^2 / \text{MSE}(\mathbf{x}')$, where $\|\mathbf{x}\|_{\infty}$ takes the largest magnitude in \mathbf{x} , and $\text{MSE}(\mathbf{x}') = \|\mathbf{x} - \mathbf{x}'\|_F^2 / n^2$.

2.1. The MSE curve and intuition

Since we do not know \mathbf{x} , we cannot access the PSNR curve or the corresponding MSE curve. But we observe

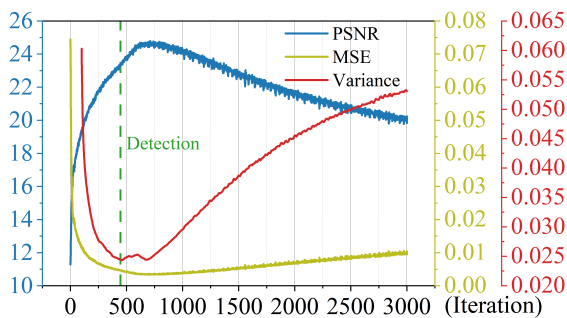


Figure 2. Relationship between the PSNR, MSE, and VAR curves. Our detection relies on the VAR curve to detect the MSE valley, and thus find the near-peak PSNR point.

that (Fig. 2) generally the MSE (resp. PSNR) curve follows a U (resp. bell) shape: $\|\mathbf{x}^t - \mathbf{x}\|$ initially drops quickly to a low level, and then climbs back due to the noise effect. This is the ELTO phenomenon we discussed in Sec. 1; we hope to detect the valley of this U-shaped MSE curve.

How to gauge the shape of the MSE curve without knowing \mathbf{x} ? We consider the following measure of dispersion, based on the elementwise p norm:

$$\text{DISP}_p(t) \doteq \frac{1}{W} \sum_{w=0}^{W-1} \|\mathbf{x}^{t+w} - \frac{1}{W} \sum_{i=0}^{W-1} \mathbf{x}^{t+i}\|_p, \quad (3)$$

which can be interpreted as generalized variance. Recall that for any $\mathbf{x}', \mathbf{x}''$, $\|\mathbf{x}' - \mathbf{x}''\|_p \approx \|\mathbf{x}' - \mathbf{x}\|_p - \|\mathbf{x}'' - \mathbf{x}\|_p$ when $\mathbf{x}' - \mathbf{x}$ and $\mathbf{x}'' - \mathbf{x}$ are nearly aligned. In the initial stage of learning, all the \mathbf{x}^t 's are distant from \mathbf{x} and their mutual distances are small relative to their distances to \mathbf{x} , and so vectors $\mathbf{x}^t - \mathbf{x}$ are nearly aligned. Thus, $\text{DISP}_p(t)$ can be approximated by

$$\begin{aligned} & \frac{1}{W} \sum_{w=0}^{W-1} \|\mathbf{x} - \frac{1}{W} \sum_{i=0}^{W-1} \mathbf{x}^{t+i}\|_p - \|\mathbf{x}^{t+w} - \mathbf{x}\|_p \\ & \approx \frac{C}{W} \sum_{w=0}^{W-1} \|\mathbf{x}^{t+w} - \mathbf{x}\|_p, \end{aligned} \quad (4)$$

where the constant $C > 0$ depends on the spread of the \mathbf{x}^t 's. When the iteration is near the MSE valley, all the \mathbf{x}^t 's are near to but scattered around \mathbf{x} . So $\frac{1}{W} \sum_{i=0}^{W-1} \mathbf{x}^{t+i} \approx \mathbf{x}$ and

$$\text{DISP}_p(t) \approx \frac{1}{W} \sum_{w=0}^{W-1} \|\mathbf{x}^{t+w} - \mathbf{x}\|_p. \quad (5)$$

Although $C > 0$ likely is small, $\|\mathbf{x}^t - \mathbf{x}\|$ during the initial stage is far larger than around the valley. So combining this heuristic argument and the fact that MSE curve takes a U shape, we suspect that the $\text{DISP}_p(t)$ curve also takes a U shape, and the valleys of the two curves are nearly aligned.

2.2. Detecting transition by running variance

For convenience, we take $p = 2$ and actually square the distances—denoted as DISP_2^2 , which is effectively the running variance (VAR) of $\{\mathbf{x}^t\}_{t \geq 1}$. The heuristic argument above still follows, with slight changes to the constants. As shown in Fig. 2, the valley of the DISP_2^2 curve is indeed nicely aligned with that of the MSE. Now we only need to detect the valley of the DISP_2^2 curve. To calculate the variance, we set a window size parameter W and compute the windowed moving variance (WMV). To improve the detection robustness, we also introduce a patience number P to tolerate up to P consecutive variance stagnation. Our whole algorithmic pipeline is summarized in Algorithm 1.

2.3. Partial theoretical justification

We can make our heuristic argument in Sec. 2.1 slightly more rigorous by restricting ourselves to additive denoising, i.e., $\mathbf{y} = \mathbf{x} + \mathbf{n}$, and appealing to the popular linearization

Algorithm 1 DIP with ES-WMV

Input: random seed \mathbf{z} , randomly-initialized G_θ , window size W , patience number P , empty queue \mathcal{Q} , iteration counter $k = 0$

Output: reconstruction \mathbf{x}^*

```

1: while not stopped do
2:   update  $\theta$  via Eq. (2) to obtain  $\theta^{k+1}$  and  $\mathbf{x}^{k+1}$ 
3:   push  $\mathbf{x}^{k+1}$  to  $\mathcal{Q}$ , pop queue front if  $|\mathcal{Q}| > W$ 
4:   if  $|\mathcal{Q}| = W$  then
5:     calculate VAR of elements in  $\mathcal{Q}$ 
6:     update  $\text{VAR}_{\min}$  and the corresponding  $\mathbf{x}^*$ 
7:     if no decrease of  $\text{VAR}_{\min}$  in  $P$  consecutive iterations then
8:       stop and return  $\mathbf{x}^k$ 
9:     end if
10:  end if
11:   $k = k + 1$ 
12: end while

```

strategy (i.e., neural tangent kernel [16, 18]) in understanding DNNs. The idea is based on the assumption that during DNN training θ does not move much from initialization θ^0 , so that the learning dynamic can be approximated by that of a linearized model, i.e., suppose we take the MSE loss

$$\begin{aligned} & \|\mathbf{y} - G_\theta(\mathbf{z})\|_2^2 \\ & \approx \|\mathbf{y} - G_{\theta^0}(\mathbf{z}) - \mathbf{J}_G(\theta^0)(\theta - \theta^0)\|_2^2 \doteq \hat{f}(\theta), \end{aligned} \quad (6)$$

where $\mathbf{J}_G(\theta^0)$ is the Jacobian of G with respect to θ at θ^0 , and $G_{\theta^0}(\mathbf{z}) + \mathbf{J}_G(\theta^0)(\theta - \theta^0)$ is the first-order Taylor approximation to $G_\theta(\mathbf{z})$ around θ^0 . $\hat{f}(\theta)$ is simply a least-squares objective. We can directly calculate the running variance based on the linear model, as shown below.

Theorem 2.1. *Let σ_i 's and \mathbf{w}_i 's be the singular values and left singular vectors of $\mathbf{J}_G(\theta^0)$, and suppose we run gradient descent with step size η on the linearized objective $\hat{f}(\theta)$ to obtain $\{\theta^t\}$ and $\{\mathbf{x}^t\}$ with $\mathbf{x}^t \doteq G_{\theta^0}(\mathbf{z}) + \mathbf{J}_G(\theta^0)(\theta^t - \theta^0)$. Then provided that $\eta \leq 1/\max_i(\sigma_i^2)$, the running variance of $\{\mathbf{x}^t\}$ is*

$$\text{DISP}_2^2(t) = \sum_i C_{m,\eta,\sigma_i} \langle \mathbf{w}_i, \hat{\mathbf{y}} \rangle^2 (1 - \eta\sigma_i^2)^{2t}, \quad (7)$$

where $\hat{\mathbf{y}} = \mathbf{y} - G_{\theta^0}(\mathbf{z})$, and $C_{W,\eta,\sigma_i} \geq 0$ only depends on W , η , and σ_i for all i .

The proof can be found in Appendix A.1. Theorem 2.1 shows that if the learning rate (LR) η is sufficiently small, the WMV of $\{\mathbf{x}^t\}$ is monotonically decreasing. The result correctly predicts the initial trend, but conflicts with the climbing trend after the performance peak. This is a common limitation of the current linearization-based deep learning theory [7, 24], as the late-stage learning dynamic may deviate substantially from that of the linearized version. Another factor is that practical LR is not very small.

We can develop an upper bound for the WMV that does have a U shape, with the caveat that this is only an upper bound. To this end, we make use of Theorem 1 of [16], which can be summarized (some technical details omitted; precise statement reproduced in Appendix A.2) as follows: consider two-layer model $G_C(\mathbf{B}) = \text{ReLU}(\mathbf{U}\mathbf{B}\mathbf{C})\mathbf{v}$, where $\mathbf{C} \in \mathbb{R}^{n \times k}$ models 1×1 trainable convolutions, $\mathbf{v} \in \mathbb{R}^{k \times 1}$ contains fixed weights, \mathbf{U} is an upsampling operation, and \mathbf{B} is the fixed random seed. Let \mathbf{J} be a reference Jacobian matrix solely determined by the upsampling operation \mathbf{U} , and σ_i 's and \mathbf{w}_i 's the singular values and left singular vectors of \mathbf{J} . Assume $\mathbf{x} \in \text{span}\{\mathbf{w}_1, \dots, \mathbf{w}_p\}$. Then when η is sufficiently small, with high probability,

$$\|G_{C^t}(\mathbf{B}) - \mathbf{x}\|_2 \leq (1 - \eta\sigma_p^2)^t \|\mathbf{x}\|_2 + E(\mathbf{n}) + \varepsilon\|\mathbf{y}\|_2,$$

where $\varepsilon > 0$ is a small scalar related to the structure of the network and $E(\mathbf{n})$ is the error introduced by noise: $E^2(\mathbf{n}) \doteq \sum_{j=1}^n ((1 - \eta\sigma_j^2)^t - 1)^2 \langle \mathbf{w}_j, \mathbf{n} \rangle^2$. So if the gap $\sigma_p/\sigma_{p+1} > 1$, $\|G_{C^t}(\mathbf{B}) - \mathbf{x}\|_2$ is dominated by $(1 - \eta\sigma_p^2)^t \|\mathbf{x}\|_2$ when t is small, and then by $E(\mathbf{n})$ when t is large. But since the former decreases and the latter increases when t grows, the upper bound has a U shape with respect to t . Based on this result, we have:

Theorem 2.2. *Assume the same setting as Theorem 2 of [16]. Our WMV is upper bounded by*

$$\begin{aligned} & \frac{12}{W} \|\mathbf{x}\|_2^2 \frac{(1 - \eta\sigma_p^2)^{2t}}{1 - (1 - \eta\sigma_p^2)^2} + \\ & 12 \sum_{i=1}^n \left((1 - \eta\sigma_i^2)^{t+W-1} - 1 \right)^2 (\mathbf{w}_i^\top \mathbf{n})^2 + 12\varepsilon^2 \|\mathbf{y}\|_2^2. \end{aligned}$$

with high probability.

The exact statement and proof can be found in Appendix A.2. By similar reasoning as above, we can conclude that the upper bound in Theorem 2.2 also has a U shape.

2.4. A memory-efficient variant

While Algorithm 1 is already lightweight and effective in practice, we can slightly modify it to avoid maintaining the \mathcal{Q} and hence save memory. The trick is to use exponential moving variance (EMV), together with the calculation of exponential moving average (EMA). Note the hard window size parameter W is now replaced by the soft forgetting factor α : larger the α , smaller the impact of the history and hence a smaller effective window.

3. Experiments

We test our variance-based ES method (ES-WMV) on 3 families of visual IPs: image denoising, MRI reconstruction, and blind image deblurring, spanning both linear and

Algorithm 2 DIP with ES–WMV

Input: random seed \mathbf{z} , randomly-initialized G_θ , forgetting factor $\alpha \in (0, 1)$, patience number P , iteration counter $k = 0$, $\text{EMA}^0 = 0$, $\text{EMV}^0 = 0$,

Output: reconstruction \mathbf{x}^*

```
1: while not stopped do
2:   update  $\theta$  via Eq. (2) to obtain  $\theta^{k+1}$  and  $\mathbf{x}^{k+1}$ 
3:    $\text{EMA}^{k+1} = (1 - \alpha)\text{EMA}^k + \alpha\mathbf{x}^{k+1}$ 
4:    $\text{EMV}^{k+1} = (1 - \alpha)\text{EMV}^k + \alpha(1 - \alpha)\|\mathbf{x}^{k+1} - \text{EMA}^k\|_2^2$ 
5:   update  $\text{EMV}_{\min}$  and the corresponding  $\mathbf{x}^*$ 
6:   if no decrease of  $\text{EMV}_{\min}$  in  $P$  consecutive iterations then
7:     stop and return  $\mathbf{x}^k$ 
8:   end if
9:    $k = k + 1$ 
10: end while
```

nonlinear IPs. For image denoising, we also systematically evaluate ES-WMV on major variants of DIP that try to mitigate overfitting, including DD [14]¹, DIP-TV [4]², GP-DIP [5]³, and demonstrate ES-WMV as a reliable helper to detect good ES points, whether these methods succeed or not in removing the overfitting. We also compare ES-WMV with major competing methods, including SB [34], DF-STE [20]⁴, SV-ES [23]⁵ and DOP [45]⁶.

Our default setup for all experiments is as follows. Our DIP model is the original one from [40]⁷; the optimizer is ADAM with a learning rate 0.01. For all other models, we use their default architectures, optimizers, and hyperparameters. For ES-WMV, the default window size $W = 100$, and patience number $P = 1000$. We use both PSNR and SSIM to assess the reconstruction quality, and we report PSNR and SSIM gaps (difference between our detected and peak numbers) as an indicator of our detection performance. For most experiments, we repeat the experiments 3 times to report the mean and standard deviation; when not, we explain why. **All missing experimental details, as well as additional results, can be found in the appendix.**

3.1. Image denoising

Prior works dealing with the DIP overfitting issue mostly focus on image denoising, but typically only evaluate their methods on one or two kinds of noise with low noise levels, e.g., low-level Gaussian noise. Here, to stretch out the evaluation, we consider 4 types of noise: Gaussian, shot, impulse, and speckle. We take the classic 9-image dataset⁸, and for each noise type generate two noise levels, low and

high, i.e., level 2 and level 4 of [17], respectively.

Comparison with baseline methods It is natural to expect that no-reference image quality assessment (NR-IQA), such as the classic BRISQUE [29], NIQE [30] or state-of-the-art (SOTA) DNN-based NIMA [38] can possibly make good ES criteria. We thus set up a family of baseline methods, using each of these metrics to find optimal stopping.

The comparison between ES-WMV and these baseline methods is presented in Tabs. 1 and 2, for low- and high-level noise level, respectively. To save space, we only report the PSNR gaps but defer the SSIM gaps to the appendix. While our method enjoys favorable detection gaps (≤ 2) for most tested noise types and levels (except for Baboon, House, Kodak2 for certain noise type/level; we suspect this is due to the substantial high-frequency components in these two images), detection gaps by the baseline methods can very often get huge ≥ 10 . We hence do not report the mean and standard deviation for these methods, as it is unlikely these bad detection results are due to randomness.

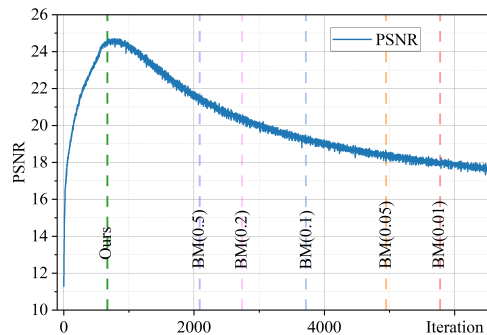


Figure 3. Comparison of SB vs ES-WMV for DIP ES detection

Comparison with competing methods We continue to compare our method with 4 main competitors: SB, DF-STE, SV-ES and DOP.

SB has not released their code yet; we are unable to reproduce their results despite best efforts. So here, we just test their ES method on DIP for Gaussian denoising with high noise; we note that the authors have acknowledged [34] their ES method does not work for DIP. DF-STE is specific for Gaussian and Poisson denoising, and the noise variance is needed for their tuning parameters. SV-ES is designed to work for all noise types and levels. DOP is designed specifically for impulse noise.

Our test of SB confirms that their blurriness metric (BM; based on the ratio of blurriness and sharpness) fails on the original DIP for Gaussian denoising; in particular, their performance is sensitive to their stopping threshold; see Fig. 3. Tab. 3 presents the comparison with DF-STE. Here, we directly report the final PSNRs obtained by both methods⁹.

⁹A technical detail we need to clarify here is: in DF-STE [20], when

¹https://github.com/reinhardt/supplement_deep_decoder
²<https://github.com/sedaboni/ADMM-DIPTV>
³<https://people.cs.umass.edu/~zezhoucheng/gp-dip/>
⁴<https://github.com/gistvision/dip-denoising>
⁵<https://github.com/sun-umn/Self-Validation>
⁶<https://github.com/ChongYou/robust-image-recovery>
⁷<https://github.com/DmitryUlyanov/deep-image-prior>
⁸http://www.cs.tut.fi/~foi/GCF-BM3D/index.html#ref_results

Table 1. **Low-level noise** detection performance. For NIMA, we report both technical quality assessment (before “/”) and aesthetic assessment (after “/”). For our method, we report both mean and (std). The **smallest PSNR gaps** within each cell are in **red**.

	Gaussian Noise				Impulse Noise				Speckle Noise				Shot Noise			
	BRIS.	NIQE	NIMA	Ours	BRIS.	NIQE	NIMA	Ours	BRIS.	NIQE	NIMA	Ours	BRIS.	NIQE	NIMA	Ours
House	25.1	5.63	27.2/27.7	1.42 (0.90)	17.2	14.7	23.1/37.4	2.97 (0.63)	8.86	8.53	1.61/11.5	0.80 (0.21)	11.3	8.98	1.87/12.6	0.84 (0.30)
Peppers	4.72	5.15	6.11/15.9	1.02 (0.16)	19.1	1.53	10.9/10.3	0.96 (0.08)	5.41	10.7	1.32/3.65	1.02 (0.45)	4.07	4.27	4.16/6.10	1.05 (0.17)
Lena	4.85	4.68	13.7/5.80	0.39 (0.17)	3.12	8.57	10.6/11.6	0.93 (0.20)	8.13	4.74	2.77/12.5	0.56 (0.02)	5.80	6.72	10.6/8.24	0.11 (0.08)
Baboon	0.20	0.96	4.47/15.1	3.87 (0.12)	0.15	0.41	5.46/17.4	4.33 (0.11)	0.43	0.69	5.03/10.4	4.31 (0.18)	0.21	1.15	4.53/2.88	3.48 (0.14)
F16	5.72	7.00	1.60/1.66	0.72 (0.14)	20.1	19.1	19.1/8.00	1.76 (0.15)	8.03	6.63	8.61/2.26	0.81 (0.47)	6.43	7.37	1.93/9.41	0.51 (0.13)
Kodak1	1.73	1.04	0.96/4.40	0.40 (0.16)	11.1	0.45	18.8/9.38	0.91 (0.11)	2.52	3.13	4.02/4.42	0.79 (0.28)	0.78	2.89	7.36/1.30	0.30 (0.08)
Kodak2	2.21	2.38	0.64 /8.45	1.62 (0.25)	3.84	3.04	12.8/17.23	1.55 (0.33)	2.54	11.8	1.31 /5.10	1.53 (0.30)	10.46	5.23	1.30 /6.41	1.35 (0.32)
Kodak3	2.43	5.80	16.7/3.12	1.39 (0.73)	9.77	7.70	29.5/14.3	2.31 (0.28)	6.33	5.76	1.07 /6.76	1.66 (0.73)	7.47	5.89	1.14 /15.3	1.46 (0.09)
Kodak12	2.28	3.04	23.3/8.24	1.63 (0.61)	6.95	1.51	0.37 /12.5	1.83 (0.27)	4.44	9.73	25.7/6.39	1.02 (0.41)	7.15	6.55	2.02/6.67	0.35 (0.21)

Table 2. **High-level noise** detection performance. For NIMA, we report both technical quality assessment (before “/”) and aesthetic assessment (after “/”). For our method, we report both mean and (std). The **smallest PSNR gaps** within each cell are in **red**.

	Gaussian Noise				Impulse Noise				Speckle Noise				Shot Noise			
	BRIS.	NIQE	NIMA	Ours	BRIS.	NIQE	NIMA	Ours	BRIS.	NIQE	NIMA	Ours	BRIS.	NIQE	NIMA	Ours
House	16.3	10.1	1.02 /15.4	1.13 (0.47)	15.6	4.94	25.2/16.8	0.35 (0.08)	10.9	7.80	1.54/21.0	0.56 (0.62)	11.8	7.72	0.39 /12.5	0.87 (0.14)
Peppers	2.91	6.07	3.69/8.12	0.60 (0.37)	5.27	2.65	7.27/13.2	0.36 (0.34)	5.28	6.84	5.47/9.53	0.35 (0.24)	3.89	6.69	1.76/7.64	0.98 (0.43)
Lena	5.68	7.79	3.08/10.3	0.27 (0.11)	8.04	8.36	8.73/17.2	0.39 (0.32)	8.62	6.54	0.73/8.94	0.50 (0.47)	6.17	7.67	0.92/8.62	0.07 (0.06)
Baboon	7.73	0.33	2.17/5.78	1.36 (0.12)	3.90	6.27	8.18/0.53	0.27 (0.09)	7.48	1.79	1.74/0.81	1.63 (0.10)	6.66	3.25	1.73/0.35	1.07 (0.26)
F16	5.17	9.10	3.75/0.89	0.44 (0.07)	9.29	1.57	7.38/2.27	0.12 (0.21)	5.65	6.39	3.59/2.13	0.31 (0.13)	3.32	5.75	1.65/0.50	0.34 (0.17)
Kodak1	8.65	2.84	15.0/3.17	1.92 (0.15)	11.0	0.22	8.32/1.74	0.82 (0.40)	0.64	6.43	1.75/3.63	2.28 (0.78)	7.45	6.08	11.0/2.83	1.81 (0.11)
Kodak2	0.66	6.11	0.64 /7.55	2.51 (0.58)	13.6	0.97	7.95/13.4	2.00 (0.28)	9.55	11.9	0.69/10.9	0.63 (0.07)	11.0	7.06	1.02 /10.6	2.46 (0.71)
Kodak3	5.61	9.11	0.37 /13.5	0.42 (0.14)	13.9	1.41	1.17/17.9	0.58 (0.33)	7.85	7.37	21.6/15.0	0.48 (0.44)	8.51	9.03	23.3/12.8	0.62 (0.24)
Kodak12	6.87	9.36	2.07/8.81	0.35 (0.29)	12.9	5.55	2.15/7.86	0.91 (0.29)	6.86	8.30	18.8/11.1	0.39 (0.34)	10.9	7.87	18.4/4.20	0.72 (0.38)

Table 3. Comparison of DF-STE and ES-WMV for Gaussian and shot noise. We report both mean and (std) for each method. The **best performance** within each cell is in **red**. Particularly, **zero** standard deviation is highlighted in **blue**.

	Low Level Noise				High Level Noise			
	Gaussian		Shot		Gaussian		Shot	
	DF-STE	Ours	DF-STE	Ours	DF-STE	Ours	DF-STE	Ours
House	32.4 (0.57)	32.2 (0.89)	25.5 (0.19)	31.7 (0.44)	17.7 (0.00)	28.0 (0.57)	13.9 (0.00)	24.4 (0.38)
Peppers	28.0 (0.13)	27.8 (0.15)	28.1 (0.14)	27.5 (0.19)	17.0 (0.00)	23.8 (0.38)	16.3 (0.00)	22.9 (0.44)
Lena	30.1 (0.10)	29.2 (0.18)	25.8 (0.30)	28.6 (0.14)	19.7 (0.00)	25.4 (0.15)	14.1 (0.00)	23.6 (0.13)
Baboon	24.0 (0.80)	19.3 (0.10)	22.0 (1.29)	19.0 (0.12)	17.3 (0.00)	19.0 (0.14)	15.3 (0.00)	18.3 (0.24)
F16	29.7 (0.13)	29.2 (0.11)	22.0 (0.00)	28.0 (0.43)	19.9 (0.00)	25.2 (0.26)	10.5 (0.00)	21.0 (0.41)
Kodak1	27.3 (0.19)	25.6 (0.16)	25.8 (0.06)	25.2 (0.11)	18.6 (0.00)	21.0 (0.18)	19.1 (0.00)	20.9 (0.08)
Kodak2	27.1 (0.07)	28.1 (0.24)	29.6 (0.27)	28.2 (0.34)	15.8 (0.00)	22.7 (0.49)	17.4 (0.00)	24.3 (0.73)
Kodak3	29.9 (0.10)	29.0 (0.69)	30.1 (0.76)	28.6 (0.04)	19.2 (0.00)	26.1 (0.14)	19.7 (0.00)	25.6 (0.46)
Kodak12	31.2 (0.12)	28.4 (0.60)	25.4 (0.14)	28.7 (0.40)	21.2 (0.00)	26.5 (0.62)	12.5 (0.00)	23.0 (0.44)

they add Gaussian or shot noise to the images, they do not perform clipping to make sure the pixel values remain in the range [0, 255]. This is not physical, and this kind of saturation is a serious type of practical noise. Following [17], we perform clipping in the data.

Table 4. **Low-level noise** detection performance. For both our method and SV-ES, we report both mean and (std). The **smallest PSNR gaps** within each cell are in **red**.

	Gaussian		Impulse		Speckle		Shot	
	Ours	SV-ES	Ours	SV-ES	Ours	SV-ES	Ours	SV-ES
House	1.42 (0.90)	0.72 (0.29)	2.97 (0.63)	1.65 (0.92)	0.80 (0.21)	0.97 (0.50)	0.84 (0.30)	0.51 (0.12)
Peppers	1.02 (0.16)	0.44 (0.15)	0.96 (0.08)	0.15 (0.06)	1.02 (0.45)	0.33 (0.21)	1.05 (0.17)	0.64 (0.13)
Lena	0.39 (0.17)	0.58 (0.12)	0.93 (0.20)	0.16 (0.04)	0.56 (0.02)	0.66 (0.24)	0.11 (0.08)	0.43 (0.23)
Baboon	3.87 (0.12)	3.90 (0.10)	4.33 (0.11)	3.34 (0.02)	4.31 (0.18)	3.97 (0.14)	3.48 (0.14)	3.01 (0.08)
F16	0.72 (0.14)	0.78 (0.06)	1.76 (0.15)	0.50 (0.19)	0.81 (0.47)	0.88 (0.11)	0.51 (0.13)	0.75 (0.14)
Kodak1	0.40 (0.16)	0.58 (0.15)	0.91 (0.11)	0.87 (0.34)	0.79 (0.28)	0.42 (0.12)	0.30 (0.08)	0.52 (0.30)
Kodak2	1.62 (0.25)	0.79 (0.23)	1.55 (0.33)	1.69 (0.21)	1.53 (0.30)	0.62 (0.08)	1.35 (0.32)	0.49 (0.26)
Kodak3	1.39 (0.73)	0.98 (0.09)	2.31 (0.28)	3.49 (0.97)	1.66 (0.73)	1.31 (0.50)	1.46 (0.09)	0.73 (0.36)
Kodak12	1.63 (0.61)	0.74 (0.20)	1.83 (0.27)	1.31 (0.17)	1.02 (0.41)	0.86 (0.39)	0.35 (0.21)	0.40 (0.08)

For low-noise level, there is no clear winner. For high-noise level, ES-WMV outperforms DF-STE by considerable margins. We stress that the right variance level is provided to DF-STE in order to tune their regularization parameters, but DF-STE stops after only very few epochs leading to the very

Table 5. Wall-clock time of DIP, SV-ES, ES-WMV and ES-EMV per epoch on *NVIDIA Tesla K40 GPU*: mean and (std).

	DIP	SV-ES	ES-WMV	ES-EMV
Time(secs)	0.448 (0.030)	13.027 (3.872)	0.301 (0.016)	0.003 (0.003)

Table 6. DIP with ES-WMV vs DOP on impulse noise: mean and (std).

	Low Level		High Level	
	Detected PSNR	Detected SSIM	Detected PSNR	Detected SSIM
DIP-ES	31.64 (5.69)	0.85 (0.18)	24.74 (3.23)	0.67 (0.19)
DOP	32.12 (4.52)	0.92 (0.07)	27.34 (3.78)	0.86 (0.10)

low performance and almost zero standard deviations—they return almost the noisy input. We do not perform any parameter tuning for ES-WMV. When it comes to the comparison with SV-ES, we present the comparison on low-level noise in Tab. 4 and on high-level in Tab. 11; their performance is largely comparable. However, both our ES-WMV and ES-EMV enjoy obvious benefits in terms of wall-clock time, shown in Tab. 5: the overheads of our ES-WMV and ES-EMV are less than 3/4 and 1/100 of the DIP update itself, while SV-ES is around 25× of that. There is no surprise: while our method only needs to update the running variance of the reconstruction in each epoch, SV-ES needs to perform one round of forward- and backward passes of the autoencoder which is much more expensive. Lastly, we compare ES-WMV with DOP on denoising impulse noise (Tab. 6). The loss is changed to ℓ_1 to account for the sparsity of the noise. In terms of the final PSNRs, DOP outperforms ES-WMV by a small gap. We note that the peak PSNR of DIP with ℓ_1 lags behind DOP by about 2 points for high noise levels.

ES-WMV as a helper DD, DIP+TV, GP-DIP represent different regularization strategies for controlling overfitting. A critical and challenging problem, however, is setting the right hyperparameters for them so that overfitting is removed while peak-level performance is preserved. So practically, these methods are not free from overfitting, especially when the noise level is high. Thus, instead of treating them as competitors, we here test if ES-WMV can reliably detect good ES points for them. We focus on Gaussian denoising, and report the results in Fig. 4 (a)-(c). ES-WMV is able to attain ≤ 1 PNSR gap for most of the cases, with few outliers. These regularizations typically change the recovery trajectory. We suspect that finetuning of our method may improve on these corner cases—we leave this as future research.

SIREN [35] is a relative of DIP models, but parameterizes x as the discretization of a continuous function: this function takes into spatial coordinates and returns the cor-

responding function values. This parameterization proves beneficial in representing visual objects with substantial high-frequency components, compared to typical CNNs models used in DIP. In this experiment, we test SIREN as a replacement of DIP models for Gaussian denoising, and summarize the results in Fig. 4 (d). ES-WMV is again able to detect near-peak performance for most images.

Performance on real-world denoising As stated from the beginning, ES-WMV is designed with real-world IPs in mind, targeting unknown noise types and levels. Given the encouraging performance above, we test it on the standard RGB track of NTIRE 2020 Real Image Denoising Challenge [1]. Just to be clear, our purpose here is not to compete with SOTA methods on this dataset—they are data-driven methods based on the training set provided in the challenge, or to prove the supremacy of DIP for denoising. We simply focus on evaluating ES-WMV in a real-world setting. So we directly test ES-WMV on the validation dataset, which comprises 1024 images of size 256×256 . Since the noise types and levels are unknown, we try both MSE, as well as the more robust ℓ_1 and Huber losses. The

Table 7. ES-WMV on real image denoising: mean and (std).

	Detected PSNR	PSNR Gap	Detected SSIM	SSIM Gap
DIP (MSE)	34.04 (3.68)	0.92 (0.83)	0.92 (0.07)	0.02 (0.04)
DIP (ℓ_1)	33.92 (4.34)	0.92 (0.59)	0.93 (0.05)	0.02 (0.02)
DIP (Huber)	33.72 (3.86)	0.95 (0.73)	0.92 (0.06)	0.02 (0.03)

results are reported in Tab. 7. We do not repeat the experiments here; the means and standard deviations are obtained over the 1024 images. Our detection gaps are mostly ≤ 1.7 in PSNR and ≤ 0.06 in SSIM, even slightly better than the above results on the simulated data. Also, the absolute PSNR and SSIM detected are surprisingly high, and the MSE loss outperforms the robust losses, strongly suggesting the noise level in the dataset may be relatively low.

3.2. MRI reconstruction

We now test ES-WMV on MRI reconstruction, a classical linear IP with a nontrivial forward mapping: $y \approx \mathcal{F}(x)$, where \mathcal{F} is the subsampled Fourier operator, and we use \approx to indicate the noise encountered in practical MRI imaging may be hybrid (e.g., additive, shot) and uncertain. Here, we take 8-fold undersampling, and parametrize x using ‘‘Conv-Decoder’’ [8], a variant of DD. Due to the heavy overparameterization, overfitting occurs and ES is needed. [8] directly set the stopping point at the 2500-th epoch, and we run our ES-WMV. We pick two random cases (C1: 1001339 and C2: 1000190) from [8], which are part of the same fastMRI dataset [46]. Fig. 5 reports the detection performance (quality measured in SSIM only, to be consistent with [8]). It is clear that ES-WMV detects near-performance for both

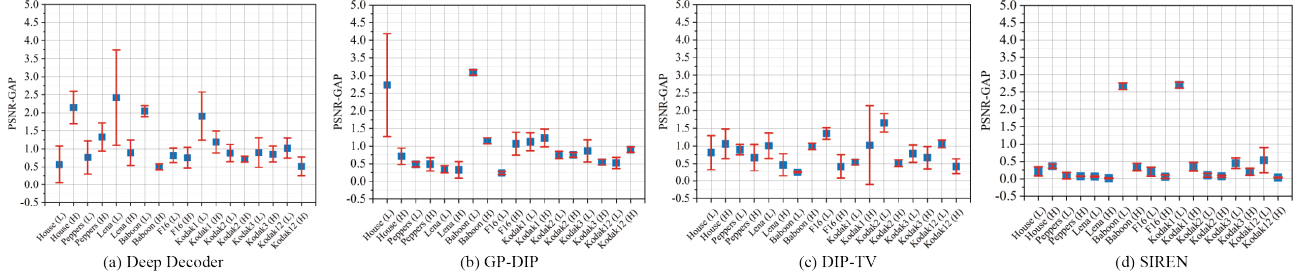


Figure 4. Performance of ES-WMV on DD, GP-DIP, DIP-TV, and SIREN for Gaussian denoising. L: low noise level; H: high noise level

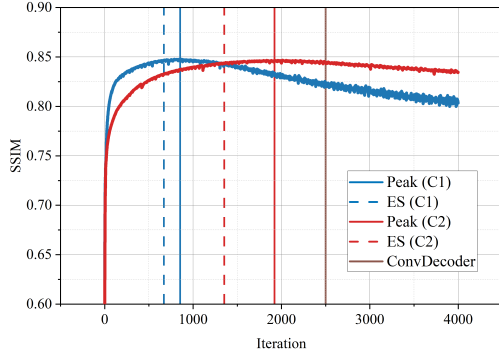


Figure 5. Detection performance on MRI reconstruction

cases, and it is adaptive enough to yield comparable or better ES points than heuristically fixing the ES point as done in ConvDecoder.

3.3. Blind image deblurring (BID)

In BID, a blurry and noisy image is given, and the goal is to recover a sharp and clean image. The blur is mostly caused by motion and/or optical nonideality in the camera, and the forward process is often modeled as $\mathbf{y} = \mathbf{k} * \mathbf{x} + \mathbf{n}$, where \mathbf{k} is blur kernel, \mathbf{n} models additive sensory noise, and $*$ is linear convolution to model the spatial uniformity of the blur effect [37]. BID is a very challenging visual IP due to the bilinearity: $(\mathbf{k}, \mathbf{x}) \mapsto \mathbf{k} * \mathbf{x}$. Recently, [2, 33, 39, 42] have tried to use DIP models to solve BID by modeling \mathbf{k} and \mathbf{x} as two separate DNNs, i.e.,

$$\min_{\theta_k, \theta_x} \|\mathbf{y} - G_{\theta_k}(\mathbf{z}_k) * G_{\theta_x}(\mathbf{z}_x)\|_2^2 + \lambda \frac{\|\nabla G_{\theta_x}(\mathbf{z}_x)\|_1}{\|\nabla G_{\theta_x}(\mathbf{z}_x)\|_2},$$

where the regularizer is to promote sparsity in the gradient domain for the reconstruction of \mathbf{x} , as is standard in BID. Here, we follow [33] and choose multi-layer perceptron (MLP) with softmax activation for G_{θ_k} , and the canonical DIP model (CNN-based encoder-decoder architecture) for $G_{\theta_x}(\mathbf{z}_x)$. We change their regularizer from the original $\|\nabla G_{\theta_x}(\mathbf{z}_x)\|_1$ to the current, as their original formulation is tested only on a very low noise level, $\sigma = 10^{-5}$ and no overfitting is observed. We set to work with higher noise

level $\sigma = 10^{-3}$, and we find that their original formulation does not work for high-level noise. The positive effect of the modified regularizer on BID has been reported before [21].

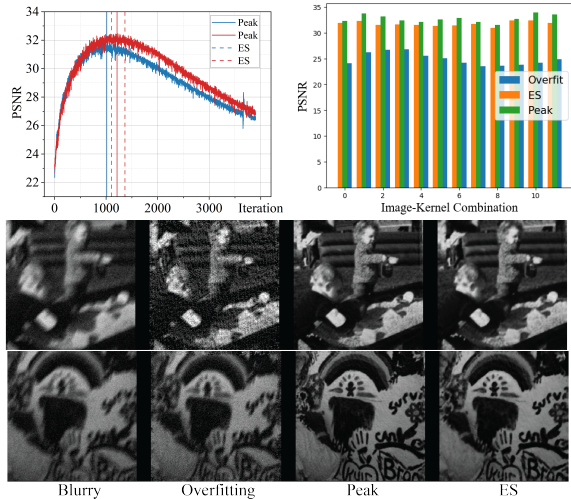


Figure 6. BID results. (top left) Example detection results on BID; (top right) Quantitative detection results on 12 image-kernel combinations; (bottom) Example recovered images

For our experiment, we take 4 images and 3 kernels from the standard Levin dataset [22], resulting in 12 image-kernel combinations. The high noise level leads to substantial overfitting, as shown in Fig. 6 (top left). Nonetheless, ES-WMV can reliably detect good ES points and lead to impressive visual reconstructions (see Fig. 6 (bottom)). Fig. 6 (top right) shows that our method returns quantitatively near-peak performance, far better than leaving the process to overfit.

3.4. Ablation study

The window size W (default 100) and patience number P (default: 1000) are the only hyperparameters for ES-WMV. To study their impact on ES detection, we vary them across a range and check how the detection gap changes for Gaussian denoising with medium-level noise, as shown in Fig. 7. Our method is quite robust against these changes,

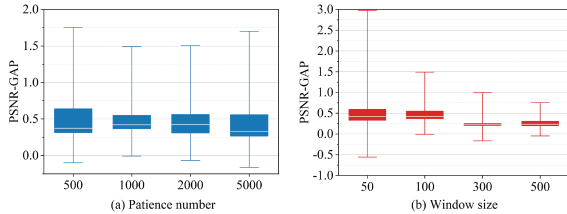


Figure 7. Effect of patience number and window size on detection

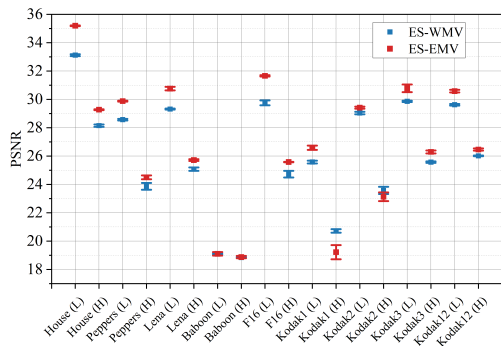


Figure 8. ES-WMV vs ES-EMV

and it seems larger W and P can bring in marginal improvement to the performance.

We now consider the our memory-efficient version (ES-EMV) as described in Algorithm 2, and compare it with ES-WMV, as shown in Fig. 8. Besides the memory benefit, ES-EMV does seem to provide consistent improvement on the detected PSNRs, due to the strong smoothing effect (we set $\alpha = 0.1$). In Appendix A.3, we show that ES-WMV on top of EMA of DIP reconstruction gets similar PSNRs. For this paper, we prefer to stay simple and leave systematic evaluations of these variants as future work.

4. Discussion and Limitations

We have proposed a simple yet effective ES detection method (ES-WMV, and the ES-EMV variant) that seems to work robustly across multiple visual IPs and DIP variants. In comparison, some competing ES methods are noise- or DIP-model-specific, and only work for limited scenarios; one competing ES method has comparable performance but it slows down the running speed too much.

Our ES method struggles with images with substantial high-frequency components. Addressing this likely requiring refining the DIP models. Our theoretical justification is only partial, sharing the same difficulty of analyzing DNNs in general. We hope to have complete comparison with the competing method SB, once we can reproduce their results.

Besides ES, there are other major technical barriers to make DIP models practical and competitive for visual IPs. A major thing is efficiency: one needs to train a DNN using

iterative methods for every instance, and there is also no natural way of performing smart initialization on θ , even if a decent α is provided.

Acknowledgement

Zhong Zhuang, Hengkang Wang, Tiancong Chen, and Ju Sun are partly supported by NSF CMMI 2038403. The authors acknowledge the Minnesota Supercomputing Institute (MSI) at the University of Minnesota for providing resources that contributed to the research results reported within this paper.

References

- [1] Abdelrahman Abdelhamed, Mahmoud Afifi, Radu Timofte, Michael S. Brown, Yue Cao, Zhilu Zhang, Wangmeng Zuo, Xiaoling Zhang, Jiye Liu, Wendong Chen, Changyuan Wen, Meng Liu, Shuailin Lv, Yunchao Zhang, Zhihong Pan, Baopu Li, Teng Xi, Yanwen Fan, Xiyu Yu, Gang Zhang, Jingtuo Liu, Junyu Han, Errui Ding, Songhyun Yu, Bumjun Park, Jechang Jeong, Shuai Liu, Ziyao Zong, Nan Nan, Chenghua Li, Zengli Yang, Long Bao, Shuangquan Wang, Dongwoon Bai, Jungwon Lee, Youngjung Kim, Kyeongha Rho, Changyeop Shin, Sungho Kim, Pengliang Tang, Yiyun Zhao, Yuqian Zhou, Yuchen Fan, Thomas Huang, Zhihao Li, Nisarg A. Shah, Wei Liu, Qiong Yan, Yuzhi Zhao, Marcin Możejko, Tomasz Latkowski, Lukasz Treszczotko, Michał Szafraniuk, Krzysztof Trojanowski, Yanhong Wu, Pablo Navarrete Michelini, Fengshuo Hu, Yunhua Lu, Sujin Kim, Wonjin Kim, Jaayeon Lee, Jang-Hwan Choi, Magauuiya Zhussip, Azamat Khassenov, Jong Hyun Kim, Hwechul Cho, Priya Kansal, Sabari Nathan, Zhangyu Ye, Xiwen Lu, Yaqi Wu, Jiangxin Yang, Yanlong Cao, Siliang Tang, Yanpeng Cao, Matteo Maggioni, Ioannis Marras, Thomas Tanay, Gregory Slabaugh, Youliang Yan, Myungjoo Kang, Han-Soo Choi, Kyungmin Song, Shusong Xu, Xiaomu Lu, Tingniao Wang, Chunxia Lei, Bin Liu, Rajat Gupta, and Vineet Kumar. Ntire 2020 challenge on real image denoising: Dataset, methods and results. *arXiv:2005.04117*, 2020. 7
- [2] Muhammad Asim, Fahad Shamsad, and Ali Ahmed. Blind image deconvolution using deep generative priors. *arXiv:1802.04073*, 2019. 2, 8
- [3] Daniel Otero Bague, Johannes Leuschner, and Maximilian Schmidt. Computed tomography reconstruction using deep image prior and learned reconstruction methods. *Inverse Problems*, 36(9):094004, Sep 2020. 2
- [4] Pasquale Cascarano, Andrea Sebastiani, Maria Colomba Comes, Giorgia Franchini, and Federica Porta. Combining weighted total variation and deep image prior for natural and medical image restoration via admm. *arXiv:2009.11380*, 2021. 2, 3, 5
- [5] Zezhou Cheng, Matheus Gadelha, Subhransu Maji, and Daniel Sheldon. A bayesian perspective on the deep image prior. In *CVPR*. IEEE, jun 2019. 2, 5
- [6] Zezhou Cheng, Matheus Gadelha, Subhransu Maji, and Daniel Sheldon. A bayesian perspective on the deep image prior. *arXiv:1904.07457*, 2019. 3

- [7] Lenaic Chizat, Edouard Oyallon, and Francis Bach. On lazy training in differentiable programming. *Advances in Neural Information Processing Systems (NeurIPS), Dec 2019, Vancouver, Canada*, Dec. 2018. 4
- [8] Mohammad Zalbagi Darestani and Reinhard Heckel. Accelerated mri with un-trained neural networks. *IEEE Transactions on Computational Imaging*, 7:724–733, 2021. 2, 7
- [9] Lijun Ding, Liwei Jiang, Yudong Chen, Qing Qu, and Zhihui Zhu. Rank overspecified robust matrix recovery: Subgradient method and exact recovery. *arXiv:2109.11154*, Sept. 2021. 2
- [10] Yosef Gandselman, Assaf Shocher, and Michal Irani. ”double-dip”: Unsupervised image decomposition via coupled deep-image-priors. In *CVPR*, June 2019. 2
- [11] Kuang Gong, Ciprian Catana, Jinyi Qi, and Quanzheng Li. Direct reconstruction of linear parametric images from dynamic pet using nonlocal deep image prior. *arXiv:2106.10359*, 2021. 2
- [12] Paul Hand, Oscar Leong, and Vladislav Voroninski. Phase retrieval under a generative prior. *arXiv:1807.04261*, 2018. 2
- [13] Fumio Hashimoto and Kibo Ote. Direct pet image reconstruction incorporating deep image prior and a forward projection model. *arXiv:2109.00768*, 2021. 2
- [14] Reinhard Heckel and Paul Hand. Deep decoder: Concise image representations from untrained non-convolutional networks. *arXiv preprint arXiv:1810.03982*, 2018. 2, 3, 5
- [15] Reinhard Heckel and Mahdi Soltanolkotabi. Compressive sensing with un-trained neural networks: Gradient descent finds a smooth approximation. In Hal Daumé III and Aarti Singh, editors, *Proceedings of the 37th International Conference on Machine Learning*, volume 119 of *Proceedings of Machine Learning Research*, pages 4149–4158. PMLR, 13–18 Jul 2020. 2
- [16] Reinhard Heckel and Mahdi Soltanolkotabi. Denoising and regularization via exploiting the structural bias of convolutional generators. In *ICLR*, 2020. 2, 4, 13
- [17] Dan Hendrycks and Thomas Dietterich. Benchmarking neural network robustness to common corruptions and perturbations. *Proceedings of the International Conference on Learning Representations*, 2019. 5, 6, 14
- [18] Arthur Jacot, Franck Gabriel, and Clément Hongler. Neural tangent kernel: Convergence and generalization in neural networks. In *Advances in neural information processing systems (pp. 8571-8580) 2018*, June 2018. 4
- [19] Joel Janai, Fatma Güney, Aseem Behl, and Andreas Geiger. Computer vision for autonomous vehicles: Problems, datasets and state of the art. *Foundations and Trends® in Computer Graphics and Vision*, 12(1–3):1–308, 2020. 1
- [20] Yeonsik Jo, Se Young Chun, and Jonghyun Choi. Rethinking deep image prior for denoising. *arXiv:2108.12841*, 2021. 2, 5
- [21] Dilip Krishnan, Terence Tay, and Rob Fergus. Blind deconvolution using a normalized sparsity measure. In *CVPR*, pages 233–240. IEEE, 2011. 8
- [22] Anat Levin, Yair Weiss, Fredo Durand, and William T Freeman. Understanding blind deconvolution algorithms. *IEEE transactions on pattern analysis and machine intelligence*, 33(12):2354–2367, 2011. 8
- [23] Taihui Li, Zhong Zhuang, Hengyue Liang, Le Peng, Hengkang Wang, and Ju Sun. Self-validation: Early stopping for single-instance deep generative priors. In *The British Machine Vision Conference (BMVC)*, 2021. 2, 5, 15
- [24] Chaoyue Liu, Libin Zhu, and Mikhail Belkin. On the linearity of large non-linear models: when and why the tangent kernel is constant. *arXiv:2010.01092*, Oct. 2020. 4
- [25] Jiaming Liu, Yu Sun, Xiaojuan Xu, and Ulugbek S. Kamilov. Image restoration using total variation regularized deep image prior. *arXiv:1810.12864*, 2018. 2, 3
- [26] Xudong Ma, Paul Hill, and Alin Achim. Unsupervised image fusion using deep image priors. *arXiv:2110.09490*, Oct. 2021. 2
- [27] Gary Mataev, Peyman Milanfar, and Michael Elad. Deepred: Deep image prior powered by red. In *Proceedings of the IEEE/CVF International Conference on Computer Vision Workshops*, pages 0–0, 2019. 2
- [28] Christopher A. Metzler, Ali Mousavi, Reinhard Heckel, and Richard G. Baraniuk. Unsupervised learning with stein’s unbiased risk estimator. *arXiv:1805.10531*, May 2018. 2
- [29] Anish Mittal, Anush Krishna Moorthy, and Alan Conrad Bovik. No-reference image quality assessment in the spatial domain. *IEEE Transactions on image processing*, 21(12):4695–4708, 2012. 5
- [30] Anish Mittal, Rajiv Soundararajan, and Alan C Bovik. Making a “completely blind” image quality analyzer. *IEEE Signal processing letters*, 20(3):209–212, 2012. 5
- [31] Gregory Ongie, Ajil Jalal, Christopher A. Metzler, Richard G. Baraniuk, Alexandros G. Dimakis, and Rebecca Willett. Deep learning techniques for inverse problems in imaging. *IEEE Journal on Selected Areas in Information Theory*, 1(1):39–56, may 2020. 1
- [32] Adnan Qayyum, Inaam Ilahi, Fahad Shamshad, Farid Bousaid, Mohammed Bennamoun, and Junaid Qadir. Untrained neural network priors for inverse imaging problems: A survey. *TechRxiv*, mar 2021. 2
- [33] Dongwei Ren, Kai Zhang, Qilong Wang, Qinghua Hu, and Wangmeng Zuo. Neural blind deconvolution using deep priors. In *CVPR*, June 2020. 2, 8
- [34] Zenglin Shi, Pascal Mettes, Subhransu Maji, and Cees G. M. Snoek. On measuring and controlling the spectral bias of the deep image prior. *arXiv:2107.01125*, 2021. 2, 5
- [35] Vincent Sitzmann, Julien Martel, Alexander Bergman, David Lindell, and Gordon Wetzstein. Implicit neural representations with periodic activation functions. *Advances in Neural Information Processing Systems*, 33, 2020. 3, 7
- [36] Zhaodong Sun. Solving inverse problems with hybrid deep image priors: the challenge of preventing overfitting. *arXiv:2011.01748*, 2021. 2
- [37] Richard Szeliski. *Computer Vision*. Springer London, 2nd edition, 2021. 1, 8
- [38] Hossein Talebi and Peyman Milanfar. Nima: Neural image assessment. *IEEE Transactions on Image Processing*, 27(8):3998–4011, 2018. 5

- [39] Phong Tran, Anh Tuan Tran, Quynh Phung, and Minh Hoai. Explore image deblurring via encoded blur kernel space. In *CVPR*. IEEE, jun 2021. [2](#), [8](#)
- [40] Dmitry Ulyanov, Andrea Vedaldi, and Victor Lempitsky. Deep image prior. In *CVPR*, pages 9446–9454, 2018. [1](#), [2](#), [5](#)
- [41] Dave Van Veen, Ajil Jalal, Mahdi Soltanolkotabi, Eric Price, Sriram Vishwanath, and Alexandros G. Dimakis. Compressed sensing with deep image prior and learned regularization. *arXiv:1806.06438*, 2020. [2](#)
- [42] Zhunxuan Wang, Zipei Wang, Qiqi Li, and Hakan Bilen. Image deconvolution with deep image and kernel priors. *arXiv:1910.08386*, 2019. [2](#), [8](#)
- [43] Francis Williams, Teseo Schneider, Claudio Silva, Denis Zorin, Joan Bruna, and Daniele Panozzo. Deep geometric prior for surface reconstruction. *arXiv:1811.10943*, 2019. [2](#)
- [44] Jaejun Yoo, Kyong Hwan Jin, Harshit Gupta, Jerome Yerly, Matthias Stuber, and Michael Unser. Time-dependent deep image prior for dynamic mri. *arXiv:1910.01684*, 2021. [2](#)
- [45] Chong You, Zhihui Zhu, Qing Qu, and Yi Ma. Robust recovery via implicit bias of discrepant learning rates for double over-parameterization. *arXiv:2006.08857*, 2020. [2](#), [5](#)
- [46] Jure Zbontar, Florian Knoll, Anuroop Sriram, Tullie Murrell, Zhengnan Huang, Matthew J. Muckley, Aaron Defazio, Ruben Stern, Patricia Johnson, Mary Bruno, Marc Parente, Krzysztof J. Geras, Joe Katsnelson, Hersh Chandarana, Zizhao Zhang, Michal Drozdal, Adriana Romero, Michael Rabbat, Pascal Vincent, Nafissa Yakubova, James Pinkerton, Duo Wang, Erich Owens, C. Lawrence Zitnick, Michael P. Recht, Daniel K. Sodickson, and Yvonne W. Lui. fastmri: An open dataset and benchmarks for accelerated mri. *arXiv:1811.08839*, Nov. 2018. [7](#)

A. Appendix

A.1. Proof of Theorem 2.1

Proof. To simplify the notation, we write $\hat{\mathbf{y}} \doteq \mathbf{y} - G_{\theta^0}(\mathbf{z})$, $\mathbf{J} \doteq \mathbf{J}_G(\theta^0)$, and $\mathbf{c} \doteq \boldsymbol{\theta} - \theta^0$. So the least-squares objective in Eq. (6) is equivalent to

$$\|\hat{\mathbf{y}} - \mathbf{J}\mathbf{c}\|_2^2 \quad (8)$$

and the gradient update reads

$$\mathbf{c}^t = \mathbf{c}^{t-1} - \eta \mathbf{J}^\top (\mathbf{J}\mathbf{c}^{t-1} - \hat{\mathbf{y}}), \quad (9)$$

where $\mathbf{c}^0 = \mathbf{0}$ and $\mathbf{x}^t = \mathbf{J}\mathbf{c}^t + G_{\theta^0}(\mathbf{z})$. The residual at time t can be computed as

$$\mathbf{r}^t \doteq \hat{\mathbf{y}} - \mathbf{J}\mathbf{c}^t \quad (10)$$

$$= \hat{\mathbf{y}} - \mathbf{J}(\mathbf{c}^{t-1} - \eta \mathbf{J}^\top (\mathbf{J}\mathbf{c}^{t-1} - \hat{\mathbf{y}})) \quad (11)$$

$$= (\mathbf{I} - \eta \mathbf{J}\mathbf{J}^\top) (\hat{\mathbf{y}} - \mathbf{J}\mathbf{c}^{t-1}) \quad (12)$$

$$= (\mathbf{I} - \eta \mathbf{J}\mathbf{J}^\top)^2 (\hat{\mathbf{y}} - \mathbf{J}\mathbf{c}^{t-2}) = \dots \quad (13)$$

$$= (\mathbf{I} - \eta \mathbf{J}\mathbf{J}^\top)^t (\hat{\mathbf{y}} - \mathbf{J}\mathbf{c}^0) \quad (\text{using } \mathbf{c}^0 = \mathbf{0}) \quad (14)$$

$$= (\mathbf{I} - \eta \mathbf{J}\mathbf{J}^\top)^t \hat{\mathbf{y}}. \quad (15)$$

Assume the SVD of \mathbf{J} as $\mathbf{J} = \mathbf{W}\boldsymbol{\Sigma}\mathbf{V}^\top$. Then

$$\mathbf{r}^t = (\mathbf{I} - \eta \mathbf{W}\boldsymbol{\Sigma}^2\mathbf{W}^\top)^t \hat{\mathbf{y}} = \sum_i (1 - \eta\sigma_i^2)^t \mathbf{w}_i^\top \hat{\mathbf{y}} \mathbf{w}_i \quad (16)$$

and so

$$\mathbf{J}\mathbf{c}^t = \hat{\mathbf{y}} - \mathbf{r}^t = \sum_i \left(1 - (1 - \eta\sigma_i^2)^t\right) \mathbf{w}_i^\top \hat{\mathbf{y}} \mathbf{w}_i. \quad (17)$$

Consider a set of W vectors $\mathcal{V} = \{\mathbf{v}_1, \dots, \mathbf{v}_W\}$. We have that the empirical variance

$$\text{VAR}(\mathcal{V}) = \frac{1}{W} \sum_{w=1}^W \left\| \mathbf{v}_w - \frac{1}{W} \sum_{j=1}^W \mathbf{v}_j \right\|_2^2 = \frac{1}{W} \sum_{w=1}^W \|\mathbf{v}_w\|_2^2 - \left\| \frac{1}{W} \sum_{w=1}^W \mathbf{v}_w \right\|_2^2. \quad (18)$$

So the variance of the set $\{\mathbf{x}^t, \mathbf{x}^{t+1}, \dots, \mathbf{x}^{t+W-1}\}$, same as the variance of the set $\{\mathbf{J}\mathbf{c}^t, \mathbf{J}\mathbf{c}^{t+1}, \dots, \mathbf{J}\mathbf{c}^{t+W-1}\}$, can be calculated as

$$\frac{1}{W} \sum_{w=0}^{W-1} \sum_i (\mathbf{w}_i^\top \hat{\mathbf{y}})^2 \left(1 - (1 - \eta\sigma_i^2)^{t+w}\right)^2 - \frac{1}{W^2} \sum_i (\mathbf{w}_i^\top \hat{\mathbf{y}})^2 \left(\sum_{w=0}^{W-1} 1 - (1 - \eta\sigma_i^2)^{t+w}\right)^2 \quad (19)$$

$$= \frac{1}{W^2} \sum_i (\mathbf{w}_i^\top \hat{\mathbf{y}})^2 \left[W \sum_{w=0}^{W-1} \left(1 - (1 - \eta\sigma_i^2)^{t+w}\right)^2 - \left(\sum_{w=0}^{W-1} 1 - (1 - \eta\sigma_i^2)^{t+w}\right)^2 \right] \quad (20)$$

$$= \frac{1}{W^2} \sum_i (\mathbf{w}_i^\top \hat{\mathbf{y}})^2 \left[\left(W^2 + W \frac{(1 - \eta\sigma_i^2)^{2t} (1 - (1 - \eta\sigma_i^2)^{2W})}{1 - (1 - \eta\sigma_i^2)^2} - 2W \frac{(1 - \eta\sigma_i^2)^t (1 - (1 - \eta\sigma_i^2)^W)}{\eta\sigma_i^2} \right) \right. \\ \left. - \left(W^2 - 2W \frac{(1 - \eta\sigma_i^2)^t (1 - (1 - \eta\sigma_i^2)^W)}{\eta\sigma_i^2} + \frac{(1 - \eta\sigma_i^2)^{2t} (1 - (1 - \eta\sigma_i^2)^W)^2}{\eta^2 \sigma_i^4} \right) \right] \quad (21)$$

$$= \frac{1}{W^2} \sum_i \langle \mathbf{w}_i, \hat{\mathbf{y}} \rangle^2 \frac{(1 - \eta\sigma_i^2)^{2t}}{\eta\sigma_i^2} \left[W \frac{1 - (1 - \eta\sigma_i^2)^{2W}}{2 - \eta\sigma_i^2} - \frac{(1 - (1 - \eta\sigma_i^2)^W)^2}{\eta\sigma_i^2} \right]. \quad (22)$$

So the constants C_{W,η,σ_i} 's are defined as

$$C_{W,\eta,\sigma_i} \doteq \frac{1}{W^2\eta\sigma_i^2} \left[W \frac{1 - (1 - \eta\sigma_i^2)^{2W}}{2 - \eta\sigma_i^2} - \frac{(1 - (1 - \eta\sigma_i^2)^W)^2}{\eta\sigma_i^2} \right]. \quad (23)$$

To see they are nonnegative, it is sufficient to show that

$$W \frac{1 - (1 - \eta\sigma_i^2)^{2W}}{2 - \eta\sigma_i^2} - \frac{(1 - (1 - \eta\sigma_i^2)^W)^2}{\eta\sigma_i^2} \geq 0 \iff \eta\sigma_i^2 W (1 - (1 - \eta\sigma_i^2)^{2W}) - (2 - \eta\sigma_i^2)(1 - (1 - \eta\sigma_i^2)^W)^2 \geq 0.$$

Now consider the function

$$h(\xi, W) = \xi W (1 - (1 - \xi)^{2W}) - (2 - \xi)(1 - (1 - \xi)^W)^2 \quad \xi \in [0, 1], W \geq 1. \quad (24)$$

First, one can easily check that $\partial_W h(\xi, W) \geq 0$ for all $W \geq 1$ and all $\xi \in [0, 1]$, i.e., $h(\xi, W)$ is monotonically increasing with respect to W . Thus, in order to prove $C_{W,\eta,\sigma_i} \geq 0$, it suffices to show that $h(\xi, 1) \geq 0$. Now

$$h(\xi, 1) = \xi(1 - (1 - \xi)^2) - (2 - \xi)\xi^2 = 0, \quad (25)$$

completing the proof. \square

A.2. Proof of Theorem 2.2

We first restate Theorem 2 in [16].

Theorem A.1 ([16]). *Let $\mathbf{x} \in \mathbb{R}^n$ be a signal in the span of the first p trigonometric basis functions, and consider a noisy observation $\mathbf{y} = \mathbf{x} + \mathbf{n}$, where the noise $\mathbf{n} \sim \mathcal{N}(\mathbf{0}, \xi^2/n \cdot \mathbf{I})$. To denoise this signal, we fit a two-layer generator network $G_{\mathcal{C}}(\mathbf{B}) = \text{ReLU}(\mathbf{U}\mathbf{B}\mathbf{C})\mathbf{v}$, where $\mathbf{v} = [1, \dots, 1, -1, \dots, -1]/\sqrt{k}$, and $\mathbf{B} \sim_{iid} \mathcal{N}(0, 1)$, and \mathbf{U} is an upsampling operator that implements circular convolution with a given kernel \mathbf{u} . Denote $\sigma \doteq \|\mathbf{u}\|_2 |\mathbf{F}g(\mathbf{u} \otimes \mathbf{u}/\|\mathbf{u}\|_2^2)|^{1/2}$ where $g(t) = (1 - \cos^{-1}(t)/\pi)t$ and \otimes denotes the circular convolution. Fix any $\varepsilon \in (0, \sigma_p/\sigma_1]$, and suppose $k \geq C_{\mathbf{u}}n/\varepsilon^8$, where $C_{\mathbf{u}} > 0$ is a constant only depending on \mathbf{u} . Consider gradient descent with step size $\eta \leq \|\mathbf{F}\mathbf{u}\|_{\infty}^{-2}$ ($\mathbf{F}\mathbf{u}$ is the Fourier transform of \mathbf{u}) starting from $\mathbf{C}_0 \sim_{iid} \mathcal{N}(0, \omega^2)$, entries, $\omega \propto \frac{\|\mathbf{y}\|_2}{\sqrt{n}}$. Then, for all iterates t obeying $t \leq \frac{100}{\eta\sigma_p^2}$, the reconstruction error obeys*

$$\|G_{\mathcal{C}^t}(\mathbf{B}) - \mathbf{x}\|_2 \leq (1 - \eta\sigma_p^2)^t \|\mathbf{x}\|_2 + \sqrt{\sum_{i=1}^n ((1 - \eta\sigma_i^2)^t - 1)^2 (\mathbf{w}_i^{\top} \mathbf{n})^2} + \varepsilon \|\mathbf{y}\|_2$$

with probability at least $1 - \exp(-k^2) - n^{-2}$.

Note that since $\mathbf{B} \sim_{iid} \mathcal{N}(0, 1)$ and hence is full-rank with probability one, the original Theorem 1 & 2 of [16] rename $\mathbf{B}\mathbf{C}$ into \mathbf{C}' and state the result directly on \mathbf{C}' , i.e., assume the model is $\text{ReLU}(\mathbf{U}\mathbf{C}')\mathbf{v}$. It is easy to see the original theorems imply the version stated here.

With this, we can obtain our **Theorem 2.2**, stated in full technical form here:

Theorem A.2. *Let $\mathbf{x} \in \mathbb{R}^n$ be a signal in the span of the first p trigonometric basis functions, and consider a noisy observation $\mathbf{y} = \mathbf{x} + \mathbf{n}$, where the noise $\mathbf{n} \sim \mathcal{N}(\mathbf{0}, \xi^2/n \cdot \mathbf{I})$. To denoise this signal, we fit a two-layer generator network $G_{\mathcal{C}}(\mathbf{B}) = \text{ReLU}(\mathbf{U}\mathbf{B}\mathbf{C})\mathbf{v}$, where $\mathbf{v} = [1, \dots, 1, -1, \dots, -1]/\sqrt{k}$, and $\mathbf{B} \sim_{iid} \mathcal{N}(0, 1)$, and \mathbf{U} is an upsampling operator that implements circular convolution with a given kernel \mathbf{u} . Denote $\sigma \doteq \|\mathbf{u}\|_2 |\mathbf{F}g(\mathbf{u} \otimes \mathbf{u}/\|\mathbf{u}\|_2^2)|^{1/2}$ where $g(t) = (1 - \cos^{-1}(t)/\pi)t$ and \otimes denotes the circular convolution. Fix any $\varepsilon \in (0, \sigma_p/\sigma_1]$, and suppose $k \geq C_{\mathbf{u}}n/\varepsilon^8$, where $C_{\mathbf{u}} > 0$ is a constant only depending on \mathbf{u} . Consider gradient descent with step size $\eta \leq \|\mathbf{F}\mathbf{u}\|_{\infty}^{-2}$ ($\mathbf{F}\mathbf{u}$ is the Fourier transform of \mathbf{u}) starting from $\mathbf{C}_0 \sim_{iid} \mathcal{N}(0, \omega^2)$, entries, $\omega \propto \frac{\|\mathbf{y}\|_2}{\sqrt{n}}$. Then, for all iterates t obeying $t \leq \frac{100}{\eta\sigma_p^2}$, our WMV obeys*

$$\text{WMV} \leq \frac{12}{W} \|\mathbf{x}\|_2^2 \frac{(1 - \eta\sigma_p^2)^{2t}}{1 - (1 - \eta\sigma_p^2)^2} + 12 \sum_{i=1}^n \left((1 - \eta\sigma_i^2)^{t+W-1} - 1 \right)^2 (\mathbf{w}_i^{\top} \mathbf{n})^2 + 12\varepsilon^2 \|\mathbf{y}\|_2^2 \quad (26)$$

with probability at least $1 - \exp(-k^2) - n^{-2}$.

Proof. We make use of the basic inequality: $\|\mathbf{a} - \mathbf{b}\|_2^2 \leq 2\|\mathbf{a}\|_2^2 + 2\|\mathbf{b}\|_2^2$ for any two vectors \mathbf{a}, \mathbf{b} of compatible dimension. We have

$$\frac{1}{W} \sum_{w=0}^{W-1} \|G_{\mathcal{C}^{t+w}}(\mathbf{B}) - \frac{1}{W} \sum_{j=0}^{W-1} G_{\mathcal{C}^{t+j}}(\mathbf{B})\|_2^2 \quad (27)$$

$$= \frac{1}{W} \sum_{w=0}^{W-1} \|G_{\mathcal{C}^{t+w}}(\mathbf{B}) - \mathbf{x} + \mathbf{x} - \frac{1}{W} \sum_{j=0}^{W-1} G_{\mathcal{C}^{t+j}}(\mathbf{B})\|_2^2 \quad (28)$$

$$\leq \left(\frac{2}{W} \sum_{w=0}^{W-1} \|G_{\mathcal{C}^{t+w}}(\mathbf{B}) - \mathbf{x}\|_2^2 \right) + 2\|\mathbf{x} - \frac{1}{W} \sum_{j=0}^{W-1} G_{\mathcal{C}^{t+j}}(\mathbf{B})\|_2^2 \quad (29)$$

$$\leq \frac{2}{W} \sum_{w=0}^{W-1} \|G_{\mathcal{C}^{t+w}}(\mathbf{B}) - \mathbf{x}\|_2^2 + \frac{2}{W} \sum_{j=0}^{W-1} \|G_{\mathcal{C}^{t+j}}(\mathbf{B}) - \mathbf{x}\|_2^2 \quad (z \mapsto \|z - \mathbf{x}\|_2^2 \text{ convex and Jensen's inequality}) \quad (30)$$

$$= \frac{4}{W} \sum_{w=0}^{W-1} \|G_{\mathcal{C}^{t+w}}(\mathbf{B}) - \mathbf{x}\|_2^2. \quad (31)$$

In view of [Theorem A.1](#),

$$\|G_{\mathcal{C}^{t+w}}(\mathbf{B}) - \mathbf{x}\|_2^2 \leq 3(1 - \eta\sigma_p^2)^{2t+2w} \|\mathbf{x}\|_2^2 + 3 \sum_{i=1}^n \left((1 - \eta\sigma_j^2)^{t+w} - 1 \right)^2 (\mathbf{w}_i^\top \mathbf{n})^2 + 3\varepsilon^2 \|\mathbf{y}\|_2^2. \quad (32)$$

Thus,

$$\begin{aligned} & \sum_{w=0}^{W-1} \|G_{\mathcal{C}^{t+w}}(\mathbf{B}) - \mathbf{x}\|_2^2 \\ & \leq 3\|\mathbf{x}\|_2^2 \sum_{w=0}^{W-1} (1 - \eta\sigma_p^2)^{2t+2w} + 3 \sum_{w=0}^{W-1} \sum_{i=1}^n \left((1 - \eta\sigma_i^2)^{t+w} - 1 \right)^2 (\mathbf{w}_i^\top \mathbf{n})^2 + 3W\varepsilon^2 \|\mathbf{y}\|_2^2 \end{aligned} \quad (33)$$

$$\leq 3\|\mathbf{x}\|_2^2 \frac{(1 - \eta\sigma_p^2)^{2t} (1 - (1 - \eta\sigma_p^2)^{2W})}{1 - (1 - \eta\sigma_p^2)^2} + 3W \sum_{i=1}^n \left((1 - \eta\sigma_i^2)^{t+W-1} - 1 \right)^2 (\mathbf{w}_i^\top \mathbf{n})^2 + 3W\varepsilon^2 \|\mathbf{y}\|_2^2 \quad (34)$$

$$\leq 3\|\mathbf{x}\|_2^2 \frac{(1 - \eta\sigma_p^2)^{2t}}{1 - (1 - \eta\sigma_p^2)^2} + 3W \sum_{i=1}^n \left((1 - \eta\sigma_i^2)^{t+W-1} - 1 \right)^2 (\mathbf{w}_i^\top \mathbf{n})^2 + 3W\varepsilon^2 \|\mathbf{y}\|_2^2, \quad (35)$$

completing the proof. \square

A.3. Additional experimental details & results

Noise generation Following the noise generation rules of [\[17\]](#)¹⁰, we simulate four kinds of noise and three intensity levels for each noise type. The detailed information is as follows.

- **Gaussian noise:** 0 mean additive Gaussian noise with variance 0.12, 0.18, and 0.26 for low, medium, and high noise levels, respectively;
- **Impulse noise:** also known as salt-and-pepper noise, replacing each pixel with probability $p \in [0, 1]$ into white or black pixel with half chance each. Low, medium, and high noise levels correspond to $p = 0.3, 0.5, 0.7$, respectively;
- **Speckle noise:** for each pixel $x \in [0, 1]$, the noisy pixel is $x(1 + \varepsilon)$, where ε is 0-mean Gaussian with a variance level 0.20, 0.35, 0.45 for low, medium, and high noise levels, respectively;
- **Shot noise:** also known as Poisson noise. For each pixel $x \in [0, 1]$, the noisy pixel is Poisson distributed with rate λx , where λ is 25, 12, 5 for low, medium, and high noise levels, respectively.

¹⁰<https://github.com/hendrycks/robustness>

Image denoising We only report the PSNR results for some of experiments in [Sec. 3.1](#) to save space. The corresponding SSIM results will be shown in the rest of this section. For the comparison between ES-WMV and baseline methods, the SSIM gaps of low- and high- level noise cases are presented in [Tab. 8](#) and [Tab. 9](#), respectively. The detection gaps of our method are very marginal (< 0.02) for most noise types and levels (except for Baboon, Kodak1 and Kodak2 for certain noise type/level), while the baseline methods can well exceed 0.1 for most cases. When comparing DF-STE with ES-WMV, we record the final SSIM the two methods obtain in [Tab. 10](#). For low-noise level, ES-WMV has comparable performance with DF-STE. For high-noise level, our algorithm outperforms DF-STE by remarkable margins. In addition, the detection performance of ES-WMV on DD, GP-DIP, DIP-TV and SIREN are shown in [Fig. 9](#). Similar with the detection results in [Fig. 4](#), ES-WMV is demonstrated to be effective for most cases again. For the comparison with [\[23\]](#) for high-level noise, we can still find that ES-WMV and SV-ES have comparable performance in [Tab. 11](#).

Table 8. **Low-level noise** detection performance. For NIMA, we report both technical quality assessment (before “/”) and aesthetic assessment (after “/”). For our method, we report both mean and (std). The **smallest SSIM gaps** within each cell are in **red**.

	Gaussian Noise				Impulse Noise				Speckle Noise				Shot Noise			
	BRIS.	NIQE	NIMA	Ours	BRIS.	NIQE	NIMA	Ours	BRIS.	NIQE	NIMA	Ours	BRIS.	NIQE	NIMA	Ours
House	0.554	0.243	0.414/0.458	0.004 (0.002)	0.114	0.087	0.304/0.454	0.004 (0.001)	0.322	0.310	0.018/0.434	0.003 (0.002)	0.544	0.426	0.034/0.608	0.006 (0.002)
Peppers	0.289	0.310	0.360/0.671	0.008 (0.005)	0.820	0.004	0.198/0.166	0.002 (0.001)	0.177	0.200	0.065/0.152	0.011 (0.003)	0.229	0.235	0.237/0.315	0.012 (0.003)
Lena	0.263	0.251	0.323/0.178	0.002 (0.001)	0.012	0.059	0.108/0.135	0.002 (0.001)	0.199	0.196	0.120/0.318	0.003 (0.002)	0.316	0.364	0.321/0.446	0.002 (0.001)
Baboon	0.010	0.022	0.427/0.670	0.392 (0.014)	0.005	0.034	0.519/0.733	0.407 (0.021)	0.010	0.019	0.460/0.724	0.401 (0.013)	0.014	0.043	0.447/0.285	0.366 (0.014)
F16	0.360	0.444	0.023/0.026	0.011 (0.001)	0.489	0.450	0.477/0.052	0.002 (0.001)	0.483	0.426	0.239/0.046	0.012 (0.003)	0.438	0.485	0.040/0.240	0.012 (0.005)
Kodak1	0.037	0.019	0.081/0.369	0.014 (0.010)	0.330	0.003	0.713/0.629	0.008 (0.003)	0.058	0.078	0.335/0.374	0.030 (0.015)	0.009	0.077	0.566/0.024	0.011 (0.008)
Kodak2	0.089	0.093	0.016/0.458	0.001 (0.002)	0.023	0.081	0.207/0.532	0.005 (0.001)	0.057	0.208	0.035/0.095	0.019 (0.015)	0.234	0.180	0.011/0.257	0.001 (0.001)
Kodak3	0.158	0.392	0.427/0.208	0.000 (0.001)	0.065	0.040	0.685/0.190	0.002 (0.001)	0.233	0.196	0.013/0.264	0.004 (0.003)	0.419	0.336	0.020/0.806	0.005 (0.002)
Kodak12	0.112	0.113	0.363/0.451	0.003 (0.001)	0.036	0.002	0.006/0.154	0.003 (0.000)	0.246	0.396	0.768/0.354	0.001 (0.001)	0.411	0.383	0.108/0.387	0.003 (0.003)

Table 9. **High-level noise** detection performance. For NIMA, we report both technical quality assessment (before “/”) and aesthetic assessment (after “/”). For our method, we report both mean and (std). The **smallest SSIM gaps** within each cell are in **red**.

	Gaussian Noise				Impulse Noise				Speckle Noise				Shot Noise			
	BRIS.	NIQE	NIMA	Ours	BRIS.	NIQE	NIMA	Ours	BRIS.	NIQE	NIMA	Ours	BRIS.	NIQE	NIMA	Ours
House	0.778	0.521	0.025/0.724	0.015 (0.008)	0.365	0.038	0.864/0.673	0.002 (0.001)	0.550	0.420	0.030/0.398	0.014 (0.011)	0.736	0.602	0.051/0.712	0.007 (0.002)
Peppers	0.247	0.406	0.285/0.478	0.006 (0.004)	0.062	0.021	0.115/0.417	0.002 (0.001)	0.208	0.247	0.208/0.338	0.011 (0.005)	0.226	0.333	0.139/0.362	0.011 (0.013)
Lena	0.363	0.455	0.211/0.533	0.006 (0.000)	0.083	0.089	0.111/0.503	0.001 (0.002)	0.398	0.311	0.029/0.427	0.007 (0.008)	0.417	0.472	0.057/0.494	0.001 (0.001)
Baboon	0.559	0.024	0.336/0.430	0.221 (0.004)	0.048	0.128	0.259/0.159	0.072 (0.018)	0.557	0.054	0.265/0.109	0.224 (0.004)	0.504	0.128	0.299/0.100	0.163 (0.017)
F16	0.383	0.583	0.104/0.015	0.010 (0.003)	0.186	0.005	0.115/0.087	0.002 (0.003)	0.489	0.501	0.148/0.056	0.013 (0.008)	0.430	0.533	0.061/0.019	0.007 (0.007)
Kodak1	0.594	0.285	0.567/0.307	0.211 (0.019)	0.347	0.064	0.360/0.276	0.140 (0.032)	0.007	0.194	0.187/0.360	0.220 (0.067)	0.576	0.204	0.465/0.301	0.203 (0.014)
Kodak2	0.004	0.425	0.007/0.478	0.025 (0.001)	0.275	0.004	0.082/0.259	0.035 (0.006)	0.226	0.204	0.006 /0.263	0.008 (0.007)	0.391	0.249	0.025/0.432	0.018 (0.015)
Kodak3	0.408	0.554	0.017/0.498	0.006 (0.002)	0.275	0.010	0.007/0.547	0.002 (0.001)	0.284	0.268	0.491/0.672	0.008 (0.005)	0.449	0.475	0.731/0.392	0.005 (0.004)
Kodak12	0.409	0.484	0.140/0.471	0.005 (0.003)	0.226	0.041	0.008/0.079	0.004 (0.005)	0.431	0.467	0.254/0.643	0.003 (0.002)	0.634	0.498	0.446/0.369	0.012 (0.008)

Ablation study The SSIM gaps of changing the two hyperparameters, such as the window size W and the patience number P , are reported in [Fig. 10](#). We can draw similar conclusions that ES-WMV is rather robust against these changes and larger W and P can result in slight improvement to the performance. Next, we find that ES-EMV seems to have consistent benefits for detecting higher PSNRs in [Fig. 8](#) and suspect the reason is because of the smoothing effect. To verify this, we show that ES-WMV on the top of EMA of DIP reconstruction can obtain similar PSNRs as ES-EMV in [Fig. 11](#).

Table 10. Comparison of DF-STE and ES-WMV for Gaussian and shot noise. We report both mean and (std) for each method. The **highest SSIM** within each cell is in **red**. Particularly, **zero** standard deviation is highlighted in **blue**.

	Low Level Noise				High Level Noise			
	Gaussian		Shot		Gaussian		Shot	
	DF-STE	Ours	DF-STE	Ours	DF-STE	Ours	DF-STE	Ours
House	0.891 (0.004)	0.861 (0.006)	0.835 (0.001)	0.855 (0.008)	0.335 (0.000)	0.799 (0.006)	0.276 (0.000)	0.774 (0.009)
Peppers	0.727 (0.002)	0.724 (0.006)	0.749 (0.001)	0.728 (0.004)	0.566 (0.000)	0.623 (0.002)	0.529 (0.000)	0.640 (0.028)
Lena	0.808 (0.003)	0.792 (0.003)	0.727 (0.004)	0.777 (0.002)	0.648 (0.000)	0.672 (0.008)	0.423 (0.000)	0.667 (0.010)
Baboon	0.712 (0.015)	0.315 (0.014)	0.658 (0.034)	0.295 (0.012)	0.288 (0.000)	0.269 (0.004)	0.220 (0.000)	0.265 (0.015)
F16	0.862 (0.005)	0.844 (0.005)	0.772 (0.000)	0.816 (0.002)	0.646 (0.000)	0.776 (0.006)	0.417 (0.000)	0.722 (0.007)
Kodak1	0.777 (0.013)	0.716 (0.010)	0.749 (0.007)	0.699 (0.010)	0.349 (0.000)	0.329 (0.020)	0.345 (0.000)	0.319 (0.016)
Kodak2	0.695 (0.001)	0.717 (0.002)	0.746 (0.009)	0.713 (0.004)	0.203 (0.000)	0.575 (0.010)	0.336 (0.000)	0.585 (0.015)
Kodak3	0.828 (0.007)	0.811 (0.006)	0.846 (0.011)	0.802 (0.006)	0.636 (0.000)	0.706 (0.004)	0.630 (0.000)	0.709 (0.009)
Kodak12	0.826 (0.003)	0.762 (0.004)	0.730 (0.003)	0.744 (0.005)	0.679 (0.000)	0.679 (0.009)	0.191 (0.000)	0.649 (0.006)

Table 11. **High-level noise** detection performance. For both our method and SV-ES, we report both mean and (std). The **smallest PSNR gaps** within each cell are in **red**.

	Gaussian Noise		Impulse Noise		Speckle Noise		Shot Noise	
	Ours	SV-ES	Ours	SV-ES	Ours	SV-ES	Ours	SV-ES
House	1.13 (0.47)	0.94 (0.31)	0.35 (0.08)	0.17 (0.03)	0.56 (0.62)	0.94 (0.16)	0.87 (0.14)	1.31 (0.23)
Peppers	0.60 (0.37)	0.74 (0.36)	0.36 (0.34)	0.43 (0.05)	0.35 (0.24)	0.45 (0.23)	0.98 (0.43)	0.56 (0.13)
Lena	0.27 (0.11)	0.48 (0.16)	0.39 (0.32)	0.22 (0.04)	0.50 (0.47)	0.87 (0.10)	0.07 (0.06)	0.55 (0.18)
Baboon	1.36 (0.12)	1.55 (0.05)	0.27 (0.09)	0.16 (0.06)	1.63 (0.10)	1.44 (0.12)	1.07 (0.26)	0.92 (0.17)
F16	0.44 (0.07)	0.54 (0.12)	0.12 (0.21)	0.26 (0.05)	0.31 (0.13)	0.63 (0.33)	0.34 (0.17)	0.78 (0.21)
Kodak1	1.92 (0.15)	0.71 (0.61)	0.82 (0.40)	0.13 (0.06)	2.28 (0.78)	0.37 (0.08)	1.81 (0.11)	0.89 (0.24)
Kodak2	2.51 (0.58)	0.35 (0.05)	2.00 (0.28)	0.54 (0.37)	0.63 (0.07)	0.21 (0.09)	2.46 (0.71)	0.60 (0.06)
Kodak3	0.42 (0.14)	0.78 (0.32)	0.58 (0.33)	0.32 (0.18)	0.48 (0.44)	0.31 (0.02)	0.62 (0.24)	0.54 (0.10)
Kodak12	0.35 (0.29)	0.84 (0.17)	0.91 (0.29)	0.77 (0.32)	0.39 (0.34)	1.10 (0.25)	0.72 (0.38)	1.14 (0.21)

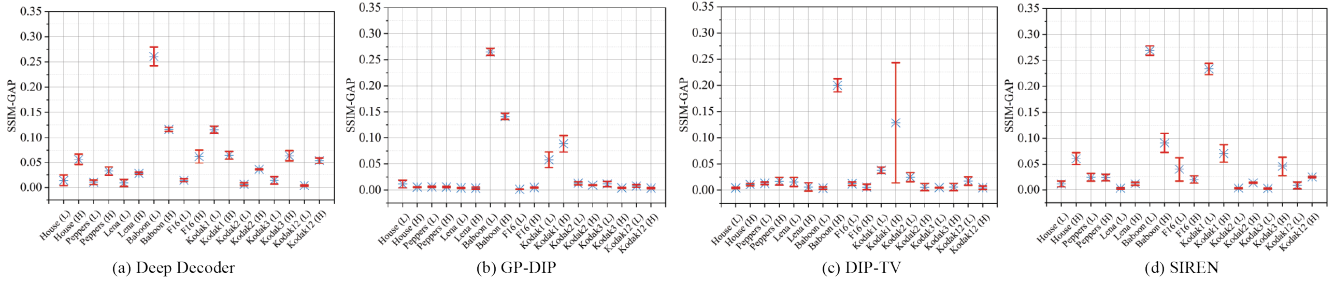


Figure 9. Performance of ES-WMV on DD, GP-DIP, DIP-TV, and SIREN for Gaussian denoising (SSIM). L: low noise level; H: high noise level

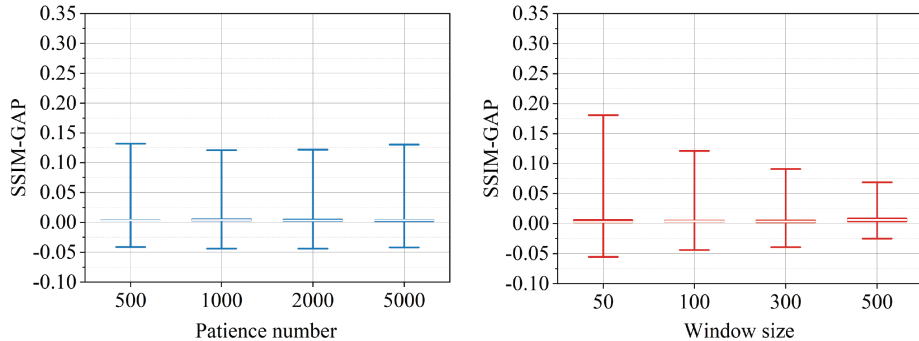


Figure 10. Effect of patience number and window size on detection (SSIM)

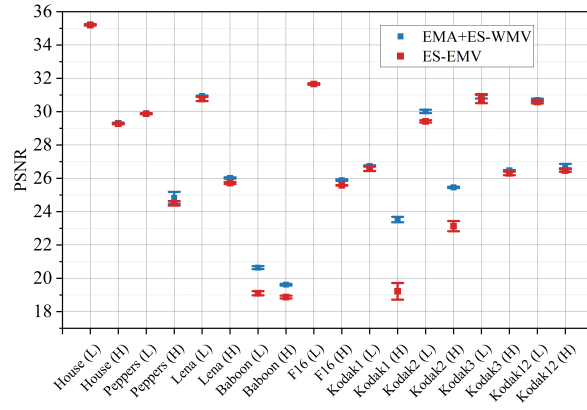


Figure 11. EMA+ES-WMV vs ES-EMV